SSRG International Journal of Electrical and Electronics Engineering
ISSN: 2348-8379/ https://doi.org/10.14445/23488379/IJEEE-V11I11P134

Volume 11 Issue 11, 360-372, November 2024

Original Article

Performance Study of a Novel Soft Switching Two Switch Enhanced Gain Modified SEPIC in Hybrid Solar-Wind Systems Featuring Battery Storage

Heena Parveen[1], A. Raghu Ram[2]

[1,2] *Department of EEE, JNTUH College of Engineering, Telangana, India.*

[1]*Corresponding Author : heenaparveen@jntuh.ac.in*

Received: 19 September 2024 Revised: 20 October 2024 Accepted: 18 November 2024 Published: 30 November 2024

Abstract *- This paper introduces a novel Soft-Switching, Two-Switch Enhanced Gain Modified SEPIC (SS-TSEGS) DC-DC converter for a Hybrid Solar-Wind System (HSWS) equipped with a battery bank storage system. The proposed converter is developed to align power production with load demand, and Zero Voltage Switching (ZVS) significantly improves its efficiency. The HSWS can work in both standalone and grid-connected modes. It provides power to DC (resistive) and AC loads (such as three-phase induction motors) in standalone mode. Power is supplied to the AC grid in grid-connected mode through a 3-ϕ Variac. To address the variability in power generation from the HSWS, a Particle Swarm Optimization-based Adaptive Neuro-Fuzzy Inference System (PSO-ANFIS) is employed for Maximum Power Point Tracking (MPPT). This ensures that the solar and wind systems generate power that is aligned with their rated capacities. A battery bank keeps the DC-link voltage constant for continuous and reliable operation. The performance of the DC/DC proposed converter and the entire hybrid system is evaluated through a simulation model designed in MATLAB/Simulink. The results demonstrate the effectiveness and efficiency of the SS-TSEGS converter in managing hybrid solar wind energy systems.*

Keywords *- Soft switching two switch enhanced gain modified SEPIC DC-DC converter, Solar system, Wind system, Battery system, DC-load, AC-load, Grid, PSO-ANFIS MPPT controller.*

1. Introduction

Global and local patterns indicate that the rising energy demand will soon be fulfilled through the widespread adoption of Renewable Energy Sources (RES). However, these sources, which depend on weather conditions, display significant spatial and temporal fluctuations. To mitigate the disparity between demand and supply from RES, a commonly suggested strategy involves combining two or more RES in a single power system, such as Wind-Solar (W-S), Solar-Hydro (S-H), or Solar-Wind-Hydro (S-W-H) configurations. The functionality of these hybrid energy systems depends on leveraging the complementary attributes of the RES [1].

Photovoltaic (PV) and wind energy have become attractive renewable energy options because they are widely available, free to use, environmentally friendly, and have low operational and maintenance costs. Due to changing environmental conditions, the variable nature of power and voltage generation poses a significant challenge for solar and wind energy. Factors like wind speed, shading, and the angle of solar insolation affect these parameters. Therefore, it is not always possible to guarantee maximum power generation for all electrical loads [2].

Wind and Solar PV systems employ various MPPT techniques to optimize the output from PV arrays and wind turbines. These techniques use controllers specifically designed to extract the maximum available power. Different MPPT methods ensure PV modules and wind turbines operate at peak performance. The efficiency of each method depends on its ability to adapt to varying weather conditions quickly. Consequently, these techniques are classified as classical, intelligent, optimization, and hybrid MPPT [3].

Here, a hybrid ANFIS is utilized as a peak power tracker. This system integrates two intelligent control methods: Artificial Neural Network (ANN) and Fuzzy Control (FC). It combines the advantages of both approaches while addressing their respective limitations, such as the need for extensive data for ANN training and the absence of fuzzy rules in Fuzzy Control. Designers face challenges in training and updating.

ANFIS specifications can be resolved using an artificial intelligence-driven Particle Swarm Optimization (PSO) technique [4]. DC to DC converters are essential in aligning the voltage output of HSWS with the specific load needs. Recent strides have concentrated on refining the SEPIC

converter to surmount conventional converter constraints. However, challenges like efficiency reduction at elevated duty cycles remain pertinent. Diverse modifications and topologies, including the "Two-Switch Enhanced Gain Modified SEPIC (TSEGS)" converter [5], aim to enhance efficiency and voltage gain.

These advancements involve integrating additional multiplier circuits and exploring various topologies, such as isolated topology, coupled inductor topology and switched capacitor technique [6-8]. Despite promising outcomes, these technologies encounter feasibility limitations attributed to efficiency, ripple content, and controllability concerns. While single-switch-based topologies have imposed control constraints, multiple-switch-based alternatives offer increased control and flexibility in managing the L-C component structure, facilitating improved voltage gain adjustment while satisfying ripple requirements.

The TSEGS converter emerges as a notable innovation, striving to reduce conduction losses and elevate overall efficiency. Yet, challenges persist, particularly regarding switching losses due to its hard-switching technique.

Consequently, soft-switching technique based TSEGS converter have been used to address this issue, maintaining high efficiency while mitigating switching losses. These advancements signify significant progress in enhancing DC-DC converter efficiency and performance, bringing us closer to achieving more reliable and efficient power conversion systems for diverse applications.

To ensure the reliable and continuous operation of a system powered by the inherently unpredictable HSWS, a battery storage system is incorporated to store excess energy when generation exceeds demand and to supply energy when generation is insufficient. This battery system comprises a battery bank and a 3-phase Interleaved Bidirectional Converter (IBC), which manages the battery's discharging and charging processes. The IBC operates in two modes: boost mode and buck mode. In boosting mode, when additional power is needed, the IBC transfers energy from the battery storage to the DC-link, providing power to the load, and the battery discharges, indicated by a positive current.

Conversely, when excess power is generated in bucking mode, the IBC moves energy from the DC link to the battery bank, charging it, and the battery current is negative. During periods of excess power generation, the HSWS produces more power than required by the load, and the surplus is directed to the battery through the IBC operating in buck mode, stepping down the voltage to a suitable level for charging. When power generation is insufficient, the IBC works in boost mode, drawing power from the battery, stepping up the voltage to the DC link level, and covering the deficit to meet load requirements.

The bidirectional converter's ability to seamlessly transition between charging and discharging optimizes battery usage and effectively balances supply and demand, ensuring reliable operation despite the HSWS's variability [9].

Two varieties of HSWS are accessible in the market: Off-Grid Systems (OGS) and Grid-Connected Systems (GCS). OGS deliver power directly to local loads, whereas GCS transmit power to the grid. This study entails the design of an HSWS capable of providing power to both local loads and the grid [10].

This research aims to design an HSWS with a battery energy system that can supply both local AC (or) DC loads and the grid. This involves regulating the HSWS output to meet load requirements by developing a high-gain, soft-switching converter. Furthermore, the research aims to maximize power extraction from the solar and wind systems using a PSO-ANFIS hybrid MPPT controller and to design a battery bank that ensures continuous and reliable system operation.

This paper is structured as follows: Section 2 covers the system layout, detailing the design of all components. Sections 3 and 4 include the simulation model, results, and discussion. Comparative analysis is presented in Section 5. Finally, the conclusion is included in Section 6.

2. System Framework

Figure 1 illustrates the block diagram of HSWS, while Table 1 details the parameter specifications of the model. The system comprises a solar arrangement, created by connecting three solar panels in series, and a wind setup, formed by linking three wind turbines in parallel.

Two separate SS-TSEGS converters are used to regulate the power output of the solar and wind systems. Furthermore, there is a battery bank equipped with a bidirectional converter to ensure continuous power operation of the system. A three-phase inverter is utilized to convert DC power to AC.

In off-grid mode, the system can power local loads, encompassing DC-load (resistive load) and AC-load (three-phase induction motor). Conversely, power is fed into the grid during grid-connected mode through the three-phase Variac. The Variac is used to align the inverter voltage with the grid voltage.

2.1. Modelling of Solar System

The Voltage-Current (V-I) cell characteristics are given by Equation (1).

$$I=I_{PV} -I_D -I_{sh} \quad (1)$$

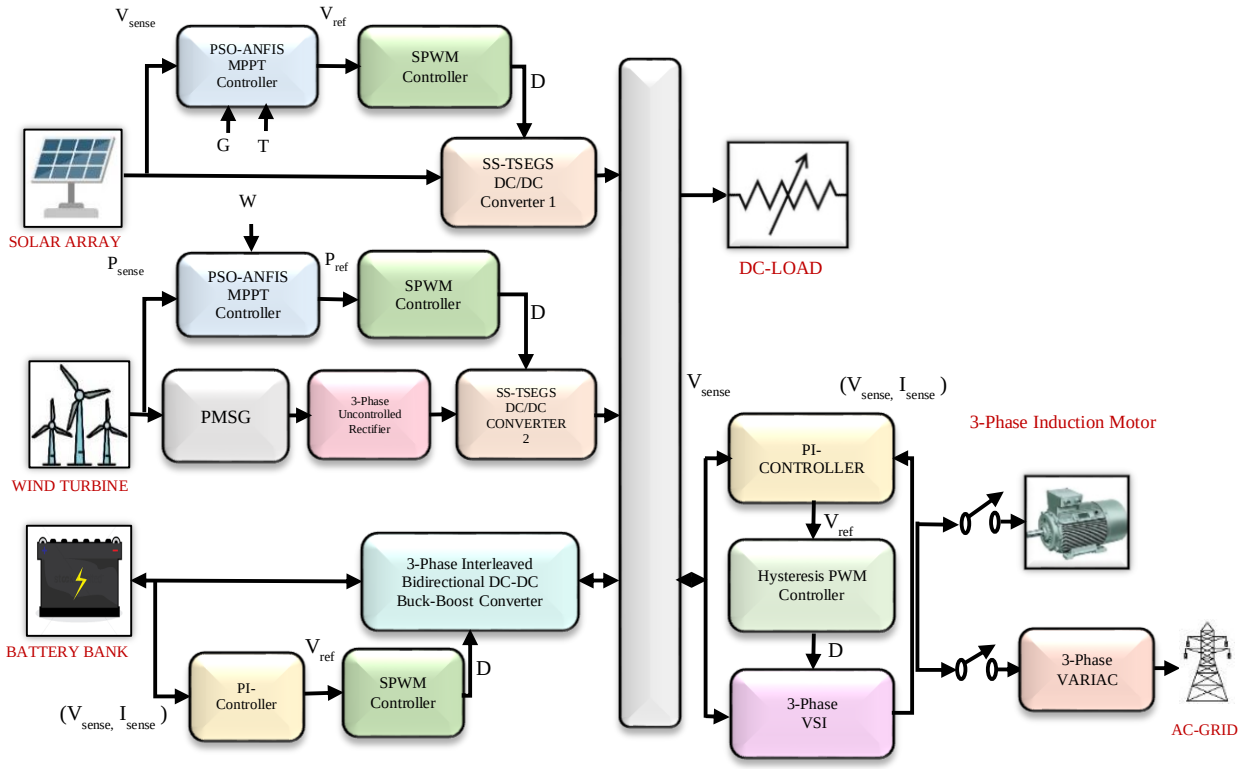

Fig. 1 System layout

$$I_D = I_o\left[e^{\frac{q(V+IR_S)}{nKN_ST}} - 1\right] \quad (2)$$

$$V_t = \frac{KN_ST}{q} \quad (3)$$

$$I_o = I_{rs}\left[\frac{T}{T_n}\right]^3\left[e^{\frac{qE_g\left[\frac{1}{T_n}-\frac{1}{T}\right]}{nK}}\right] \quad (4)$$

$$I_{PV} = [I_{sc} + K_i(T-298)]\frac{G}{G_O} \quad (5)$$

$$I_{sh} = \frac{V+IR_S}{R_{sh}} \quad (6)$$

$$I_{sc} = I_{rs}\left[e^{\frac{qV_{oc}}{nKN_ST}} - 1\right] \quad (7)$$

$$I = I_{rs}\left[e^{\frac{qV_{oc}}{nKN_ST}} - 1\right] + K_i(T-298)]\frac{G}{G_O} - I_{rs}\left[\frac{T}{T_n}\right]^3\left[e^{\frac{qE_g\left[\frac{1}{T_n}-\frac{1}{T}\right]}{nK}}\right]\left[e^{\frac{q(V+IR_S)}{nKN_ST}} - 1\right] - \left[\frac{V+IR_S}{R_{sh}}\right] \quad (8)$$

2.2. Modelling of Wind System

The wind system transforms the wind's Kinetic Energy (KE) into mechanical energy [11], as indicated by Equation (9).

$$P_m = \frac{1}{2} * C_p(\lambda, \beta) * \rho * A * V_w^3 \quad (9)$$

$$C_p = 0.5\left(\frac{116}{\lambda_i} - 0.4\beta - 5\right)e^{\left(\frac{-21}{\lambda_i}\right)} + 0.0068\lambda \quad (10)$$

$$\frac{1}{\lambda_i} = \frac{1}{\lambda + 0.08\beta} - \frac{0.035}{\beta^3 + 1} \quad (11)$$

$$\lambda = \frac{\omega R}{V_w} \quad (12)$$

$$T_m = \frac{P_m}{\omega} = \frac{\frac{1}{2} * C_p(\lambda, \beta) * \rho * A * V_w^3}{\omega} \quad (13)$$

2.3. Modelling of PMSG

The PMSG's function is to convert the rotational energy produced by the wind turbine into electrical power, with the generator's design equations outlined by Equations (14) to (22).

$$V_{sa} = e_a - R_{sa}i_{sa} - L_{sa}\frac{di_{sa}}{dt} \quad (14)$$

$$V_{sb} = e_b - R_{sb}i_{sb} - L_{sb}\frac{di_{sb}}{dt} \quad (15)$$

$$V_{sc} = e_c - R_{sc}i_{sc} - L_{sc}\frac{di_{sc}}{dt} \quad (16)$$

$$V_{sdqo} = \frac{2}{3}\begin{bmatrix} \cos\theta & \cos(\theta - \frac{2\pi}{3}) & \cos(\theta + \frac{2\pi}{3}) \\ \sin\theta & \sin(\theta - \frac{2\pi}{3}) & \sin(\theta + \frac{2\pi}{3}) \\ \frac{1}{2} & \frac{1}{2} & \frac{1}{2} \end{bmatrix} V_{sabc} \quad (17)$$

$$\theta = \int \omega_r\, dt \quad (18)$$

$$I_{sd}=\frac{1}{R_sS+L_{sd}}[V_{sd}+\omega_{dq}I_{sd}L_{sd}] \quad (19)$$

$$I_{sq}=\frac{1}{R_sS+L_s}[V_{sq}-\omega_{dq}(I_{sd}L_{sd}+\Psi)] \quad (20)$$

$$\omega_{dq}=\frac{P}{2}\omega_r=\frac{P}{2}[\frac{1}{JS+f}](T_{em}-T_m) \quad (21)$$

$$T_{em}=\frac{3}{2}P(\Psi I_{sq}+I_{sq}I_{sd}(L_{sd}-L_{sq}) \quad (22)$$

2.4. Design of Proposed Converter

Figure 2 shows the SS-TSEGS DC/DC converter. The parameter calculation formulas are given in Equation (23) to (31).

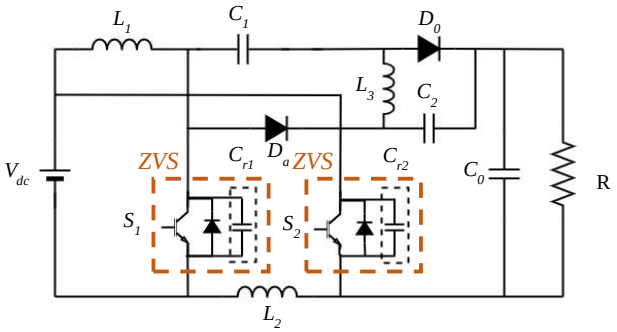

Fig. 2 Proposed DC-DC converter

The inductances L_1, L_2 and L_3 are given by Equation (23) to (25).

$$L_1 \geq \frac{DV_{in}}{\Delta i_{L1} f_s} \quad (23)$$

$$L_2 \geq \frac{DV_{in}}{\Delta i_{L2} f_s} \quad (24)$$

$$L_3 \geq \frac{2DV_{in}}{\Delta i_{L3} f_s} \quad (25)$$

The capacitances C_1, C_2 and C_O are given by Equation (26) to (28).

$$C_1 = \frac{I_0}{\Delta V_{C1} f_s} \quad (26)$$

$$C_2 = \frac{I_0}{\Delta V_{C2} f_s} \quad (27)$$

$$C_o = \frac{2DI_0}{\Delta V_{CO} f_s} \quad (28)$$

The resonant capacitors C_{r1} *and* C_{r2} are calculated using Equation (29).

$$C_{r1,r2}=\frac{D^2}{\pi^2 L_3 f_s^2} \quad (29)$$

The Soft switching effective duty cycle (D_{ss}) and gain (M_{ss}) of the converter are calculated by Equation (30) to (31).

$$D_{SS}=\frac{1}{4}[D_b(\frac{V_o}{V_{dc}}-1)-4D_c] \quad (30)$$

$$M_{SS}=\frac{V_o}{V_{in}}=\frac{1+3(D+D_c)}{1-(D+D_c)} \quad (31)$$

2.5. PSO-ANFIS MPPT Controller

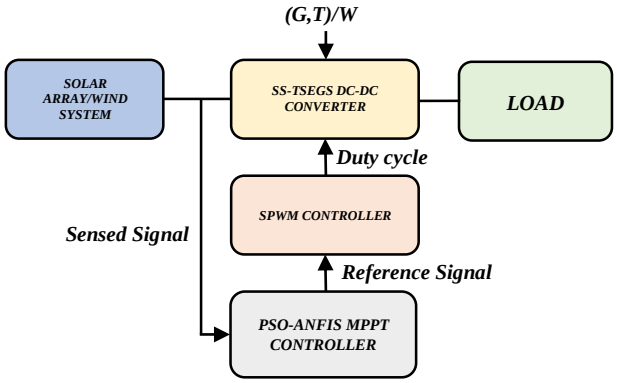

Fig. 3 Implementation of MPPT controller

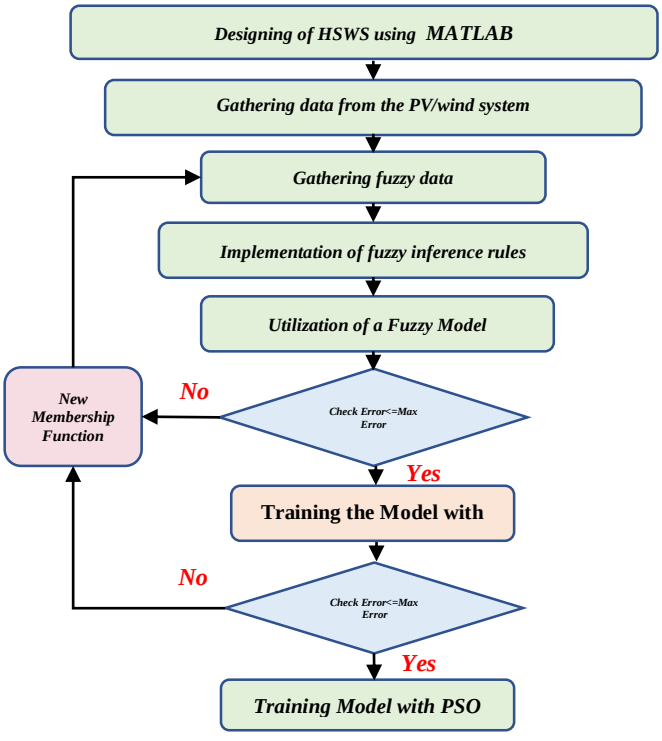

Fig. 4 Flowchart of an ANFIS–PSO-based MPPT control technique

This controller is crucial in optimizing power output from solar and wind energy systems by continually adjusting their operational settings. Utilizing an SS-TSEGS DC-DC converter, showcased in Figure 3, the PSO-ANFIS MPPT controller identifies the peak power point (MPP) and generates a corresponding reference signal for optimal voltage or power. Illustrated in Figure 4, the flow chart outlines the operational process of the PSO-ANFIS MPPT controller, which integrates PSO's optimization prowess with ANFIS's adaptive learning to pinpoint the MPP. Comparing the reference signal with a carrier signal, the PWM controller generates gating pulses, regulating the power electronic switches in the SS-TSEGS converter to align its output with the reference signal. This meticulous process ensures maximal power extraction from solar and wind sources, efficiently supplying it to the load.

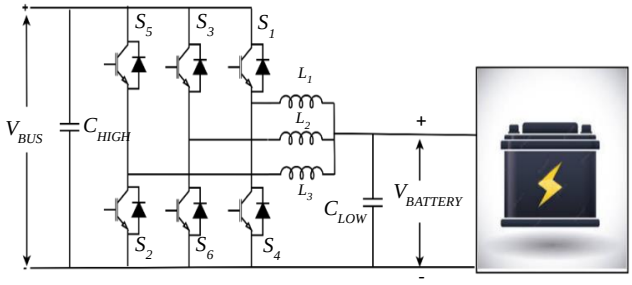

Fig. 5 Battery bank with bidirectional converter

2.6. Design of Battery System

Figure 5 depicts the diagram of a battery bank integrated with a 3-phase interleaved DC-DC bidirectional converter utilized for maintaining a constant DC-link voltage [12]. The parameter design equations for the bidirectional converter are provided in Equation (32) to (39).

$$D_{Buck}=\frac{V_L}{V_H} \tag{32}$$

$$D_{Boost}=1 - D_{Buck} \tag{33}$$

$$R_L=\frac{V_L^2}{P} \tag{34}$$

$$R_H=\frac{V_H^2}{P} \tag{35}$$

$$L_{Buck}=(1 - D_{Buck})* R_L/2/f \tag{36}$$

$$L_{Boost}= D_{Boost}*(1 - D_{Buck})* 2*R_H/2/f \tag{37}$$

$$C_L=(1 - D_{Boost}) /8/L/K_{rh}/ f^2 \tag{38}$$

$$C_H=D_{Boost} /R_L/f /K_{rl} \tag{39}$$

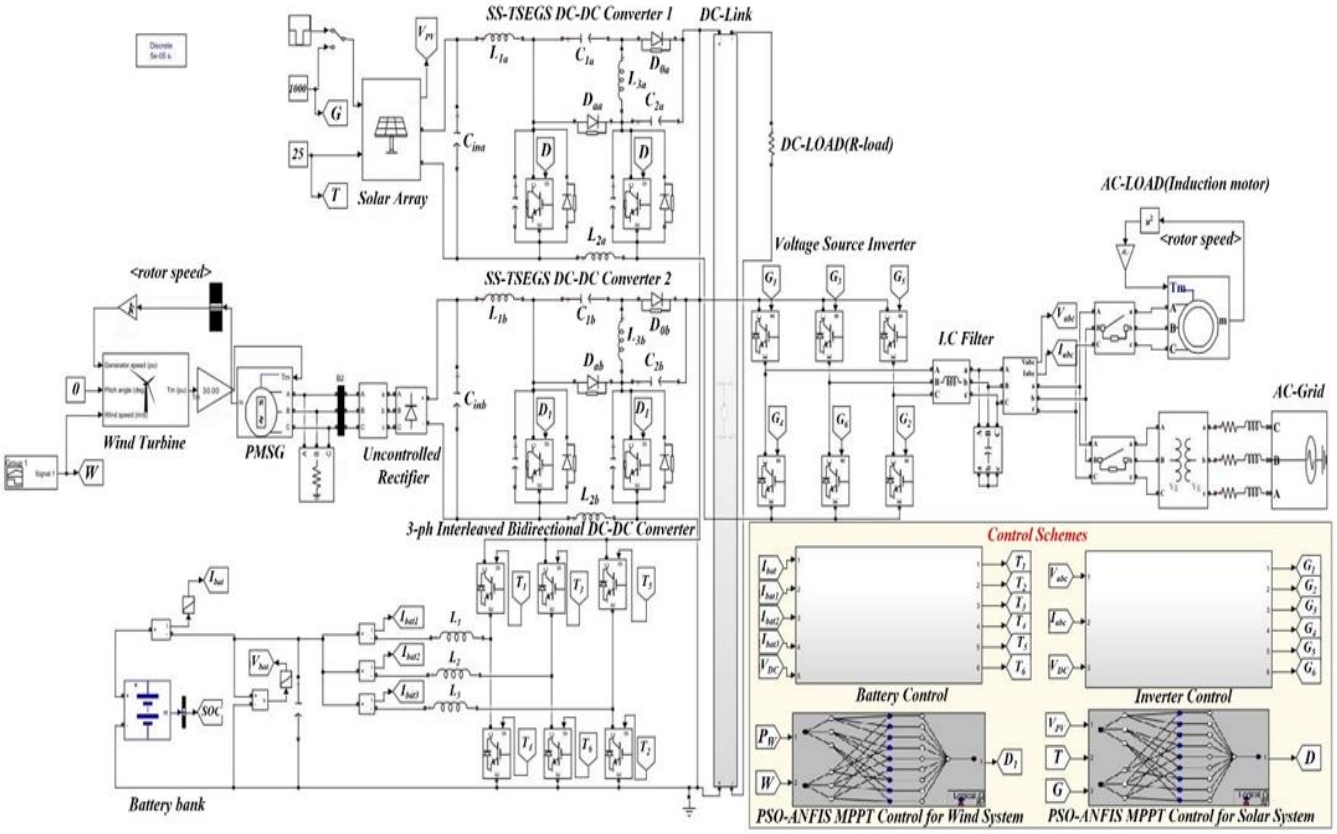

Fig. 6 Simulation model of HSWS

3. Simulation Model

Figure 6 illustrates the simulation model of HSWS, which can operate in both standalone and GC modes. The specifications of the model are detailed in Table 1. It can power resistive loads and a 3 induction motor in standalone mode. When operating in GC mode, it can supply power to the grid via a three-phase Variac. The development of the MPPT controller adheres to the process outlined in the flow chart presented in Figure 4. Meanwhile, the training of the ANFIS employing PSO entails several sequential steps.

Initially, the data is loaded into the system. Subsequently, the PSO algorithm generates the Fuzzy Inference System (FIS). Following this, the loaded data is utilized to train the system. Finally, the trained system is tested using additional data to evaluate its performance. This systematic approach ensures the effective implementation and optimization of the MPPT controller for enhanced solar and wind energy harvesting systems. The MPPT technique implemented for solar and wind systems is depicted in Figures 7 and 8.

Figure 9 illustrates the bank charging and discharging control. This battery bank upholds a constant DC-link voltage, with its charging and discharging managed through a bidirectional converter. This AC power obtained from the inverter is then supplied to either an Induction motor or the grid. The control scheme for supplying power to the induction mode is shown in Figure 10, while Figure 11 presents the control scheme for the grid-connected mode.

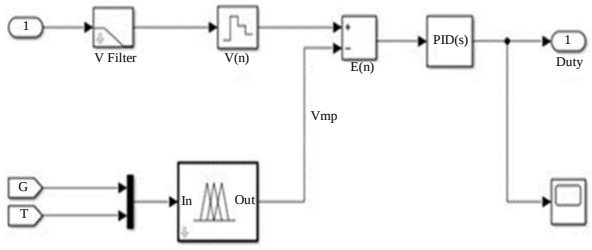

Fig. 7 Implementation of MPPT controller for solar system

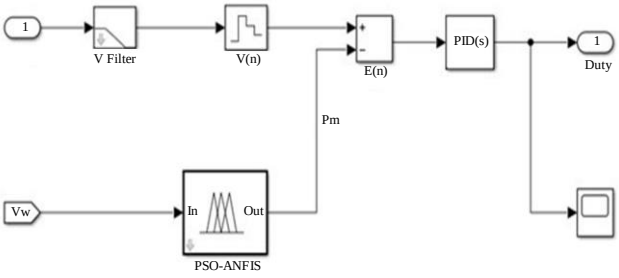

Fig. 8 Implementation of MPPT controller for wind system

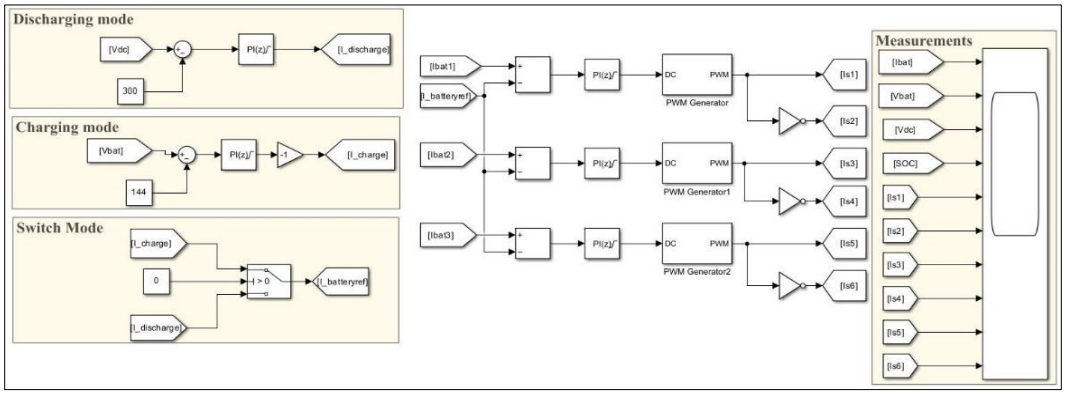

Fig. 9 Charging and discharging model of battery bank

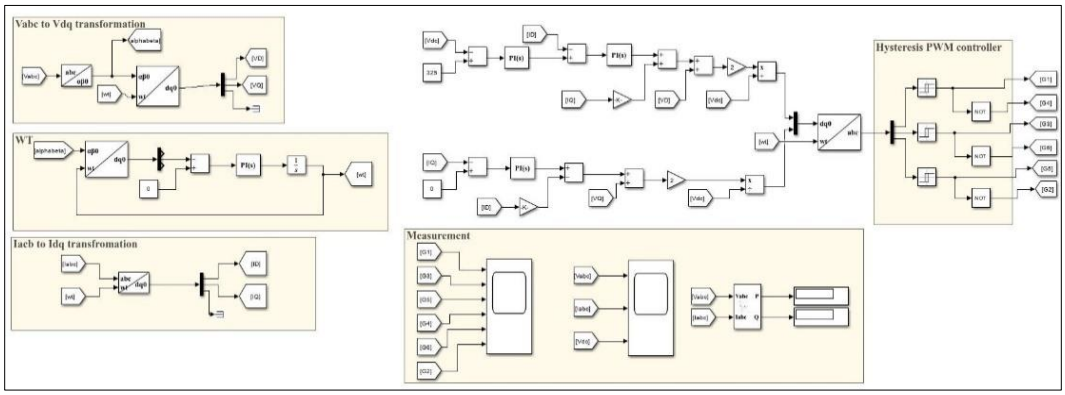

Fig. 10 Control scheme of 3-phase inverter fed induction motor

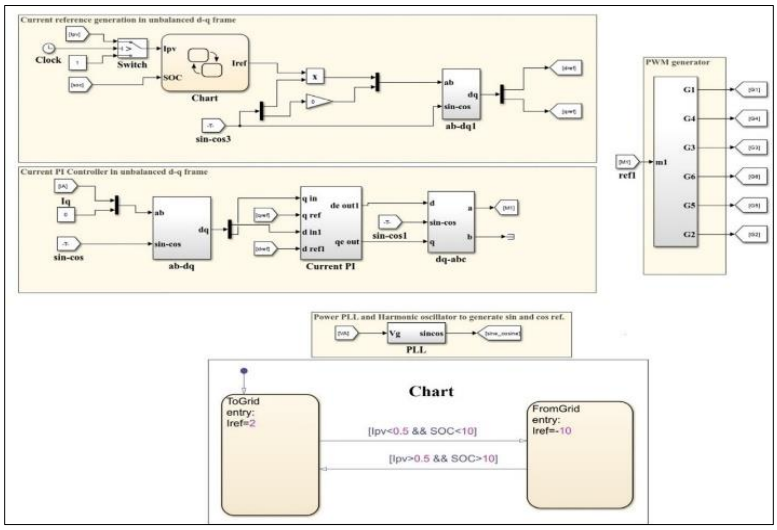

Fig. 11 Control scheme of grid connected 3-phase inverter

4. Results and Discussions

This section includes the outcomes derived from the simulation model. Figures 12 and 13 depict the solar array's Power-Voltage (PV) and Voltage-Current (VI) characteristics under various solar irradiation levels and temperatures. The figures reveal that the maximum power is generated when the solar irradiation is at 1000 W/m^{2,} and the temperature is 25°C, reaching 1006 watts. It is noted that the power output decreases with a reduction in both solar irradiation and temperature. Figure 14 displays the curve between wind speed and wind turbine output power. From the curve, it is evident that the cut-in speed of the turbine is 3 m/s, representing the minimum speed required for the turbine to rotate and produce power. The rated speed at 12 m/s corresponds to the turbine generating its rated power of 500 watts. Beyond the rated speed, as the speed increases, the turbine's output gradually decreases, reaching zero at a wind speed of 40 m/s. This speed is referred to as the cut-out speed of the turbine, indicating the threshold above which the turbine cannot generate power.

Figure 15 shows the o/p power produced by the solar PV system operating alongside an MPPT controller. It is evident from the figure that the MPPT controller ensures the solar system consistently generates power at its rated values: 1000 Watts of power output, 120 Volts of voltage, and 8.33 Amps of current. Figure 16 illustrates the power output generated by the wind system when equipped with an MPPT controller. The figure indicates that the MPPT controller effectively sustains the power output of the wind system at its rated values: 500 Watts of power, 50 Volts of voltage, and 10 Amps of current.

The MPPT technique is implemented via a proposed converter, which tracks the maximum power from both solar and wind systems. The controller generates a reference signal for the PWM controller using this information. This signal determines the gate pulses for converter switches (S1 and S2). The proposed converter's main role is to adjust the output voltage to match the generated power with the load demand, either by increasing or decreasing it Figures 17 and 18 depict the i/p and o/p waveforms of the converter used for the solar system. With the MPPT controller, the input voltage, current, and power are maintained at 120 volts, 8.3 amps, and 1000 watts, respectively.

Voltage, current, and power remain constant at 320 Volts, 3.125 amps, and 1000 watts, respectively. The converter output is managed by modulation of the switch's duty cycle. Keeping the duty cycle at 0.2939 ensures that the output voltage, current, and power remain steady at 320 Volts, 3.125 amps, and 1000 watts, respectively. Figures 19 and 20 depict the proposed converter's input and output waveforms utilized in the wind system. With the MPPT controller, the DC-DC converter maintains its input voltage, current, and power at 50 volts, 10 amps, and 500 watts, respectively. The converter output is adjusted by varying the duty cycle of the switch. A consistent duty cycle of 0.574 is upheld, ensuring that the output voltage, current, and power remain constant at 320 Volts, 3.125 amps, and 1000 watts, respectively.

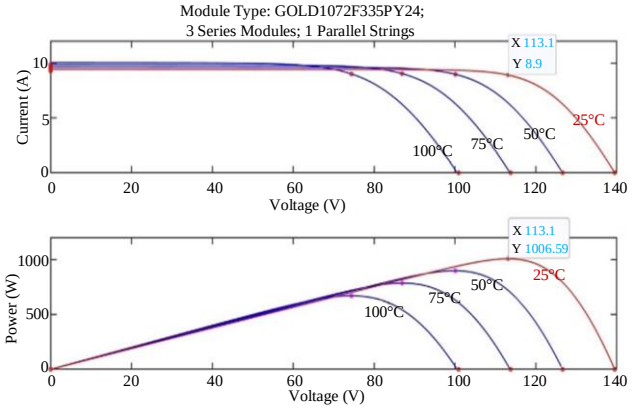

Fig. 12 PV and VI curve under different solar irradiation conditions

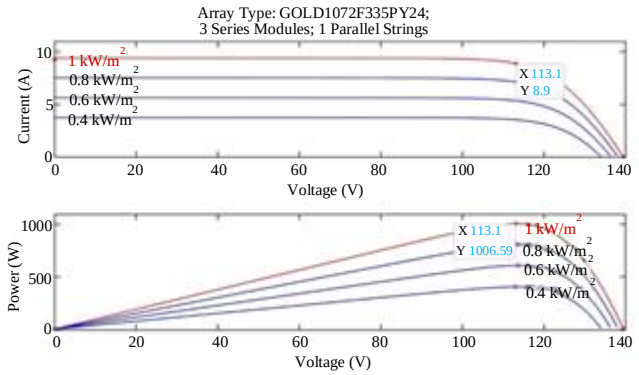

Fig. 13 PV and VI curve under different temperature conditions

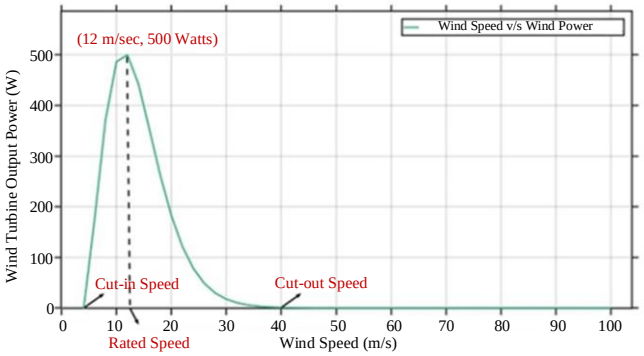

Fig. 14 Power curve for different wind speed

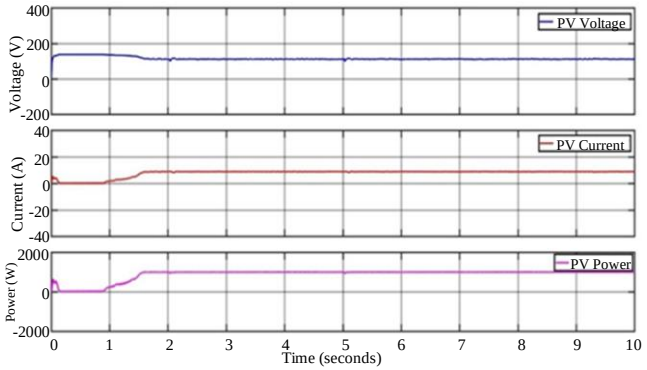

Fig. 15 Simulation outputs of solar array

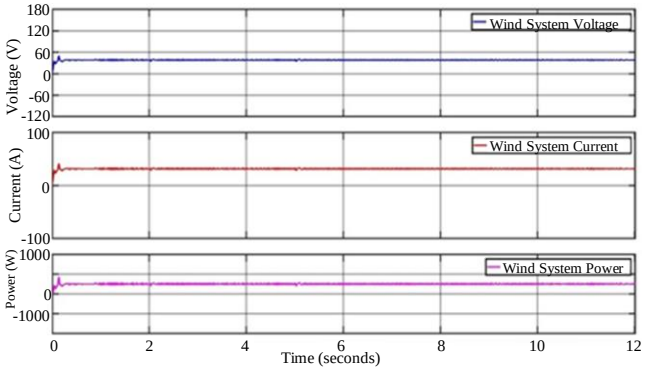

Fig. 16 Simulation outputs of wind system

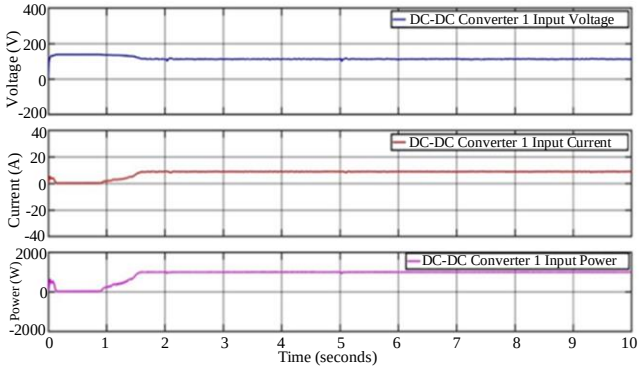

Fig. 17 Simulation input of proposed converter 1 (solar system)

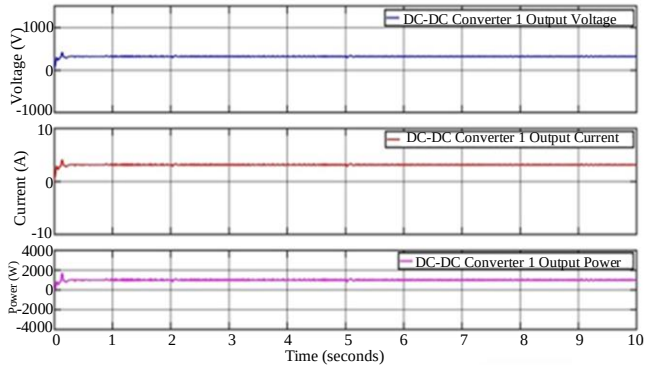

Fig. 18 Simulation waveforms of DC-DC converter 1 output (solar system)

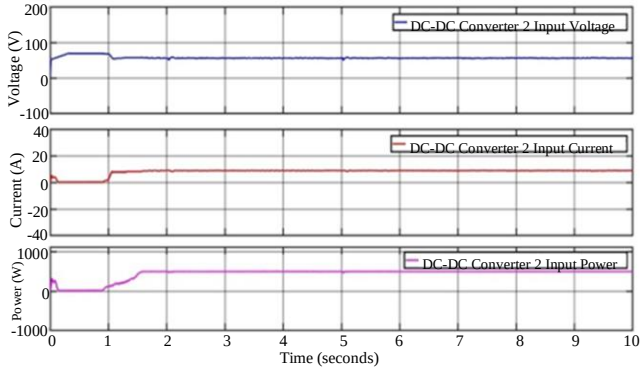

Fig. 19 Simulation input of DC-to-DC converter 2 (wind system)

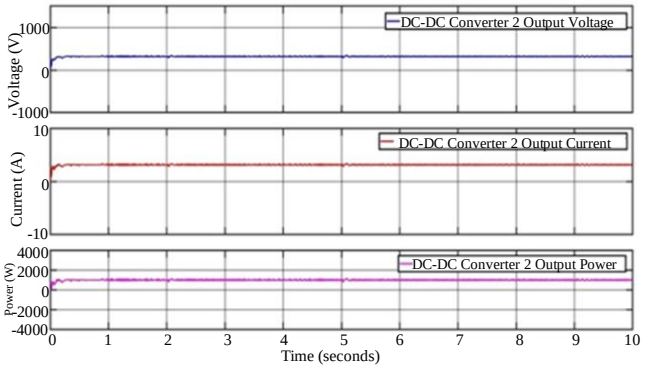

Fig. 20 Simulation output of DC/DC converter 2 (wind system)

4.1. Standalone Mode

The model supplies power to either DC-load or AC load in standalone mode.

4.1.1. DC-LOAD

A resistive DC load with a capacity of 1000 watts is connected to the DC-bus, as depicted in Figure 21. The output waveforms of the DC load are presented in Figure 22. The load is supplied with 1000 watts of power, with a DC voltage of 320 volts, and it absorbs a current of 3.125 amps.

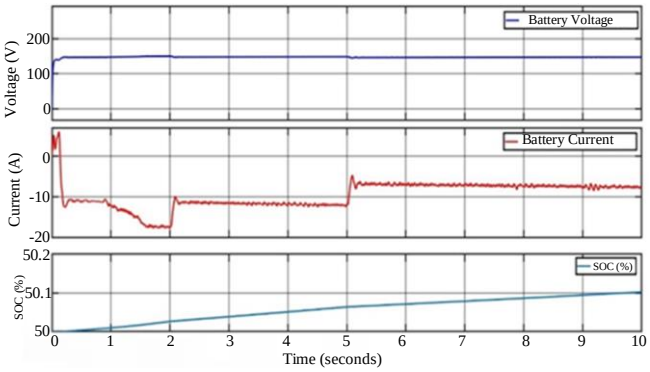

Fig. 21 Simulation outputs of battery bank

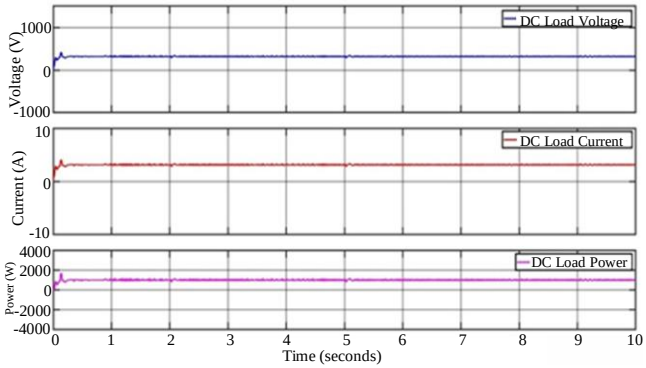

Fig. 22 Simulation outputs of DC load

4.1.2. AC LOAD

In Figure 1, a 3-ϕ induction motor is linked to the DC-link. The inverter's role is to convert DC into AC. The simulation output waveforms of the induction motor are depicted in Figure 23. These waveforms indicate that the induction motor's rotor speed, torque, and power are measured at 1400 rpm, 2.52 N-m, and 370 watts (equivalent to 0.5 horsepower).

4.2. Grid Connected Mode

In this scenario, the inverter is linked to the grid. Figure 24 displays the grid waveforms. It is clear from the figure that the grid voltage is controlled at 110 volts (line-line RMS) by employing a three-phase Variac. Furthermore, the grid current is kept at 1 ampere.

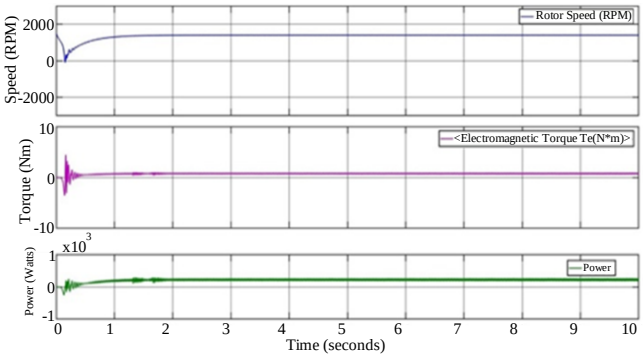

Fig. 23 Simulation outputs of AC load (3-ph induction motor)

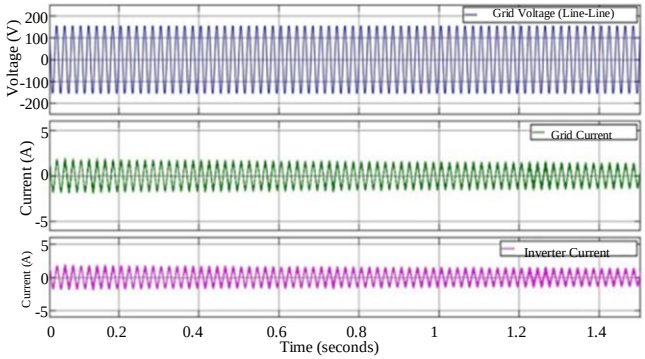

Fig. 24 Simulation output 3-phase grid

5. Comparative Analysis

Figures 25-32, it is observed that the proposed converter generates lower voltage and current THD on the load side compared to the SEPIC converter. In the case of an induction motor load, the proposed converter achieves a voltage THD of 4.43% and a current THD of 4.3%, which are lower than the voltage THD of 4.67% and current THD of 4.8% obtained with the SEPIC converter. In grid-connected mode, the proposed converter achieves a voltage THD of 0% and a current THD of 3.47%, which are lower compared to the voltage THD of 0% and current THD of 3.68% obtained with the SEPIC converter.

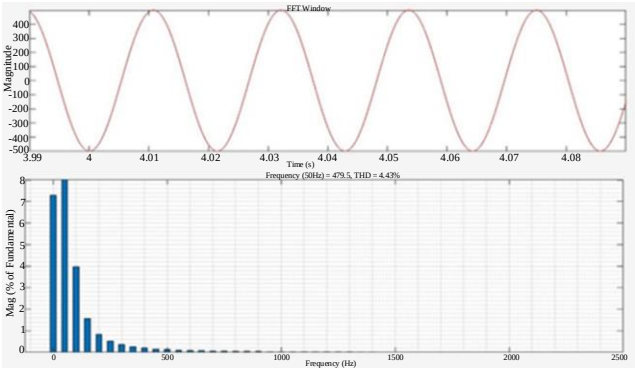

Fig. 25 Induction motor voltage THD (%) with proposed converter

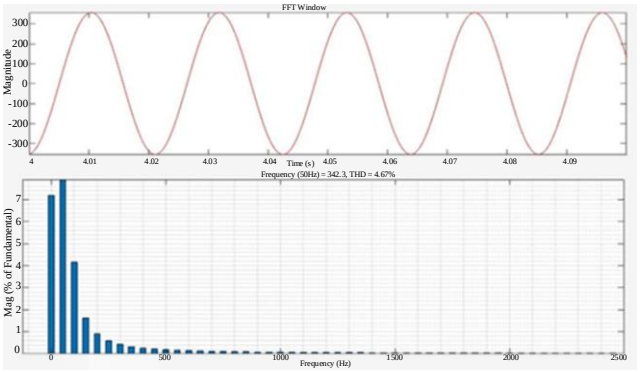

Fig. 26 Induction motor voltage THD (%) With SEPIC converter

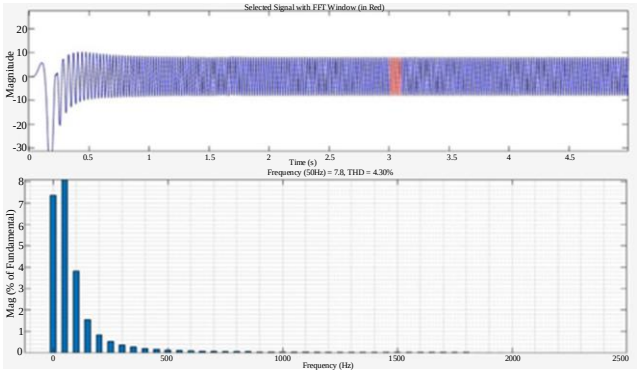

Fig. 27 Induction motor current THD (%) With proposed converter

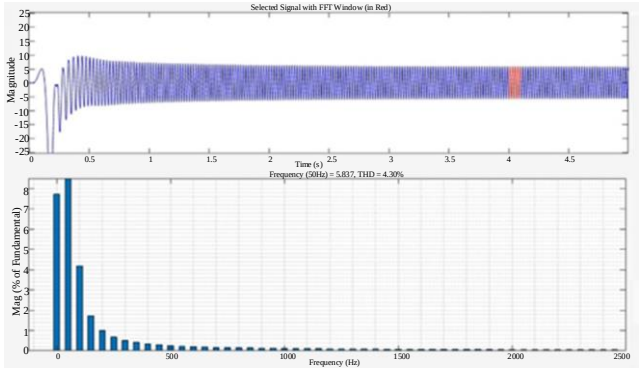

Fig. 28 Induction motor current THD (%) With SEPIC converter

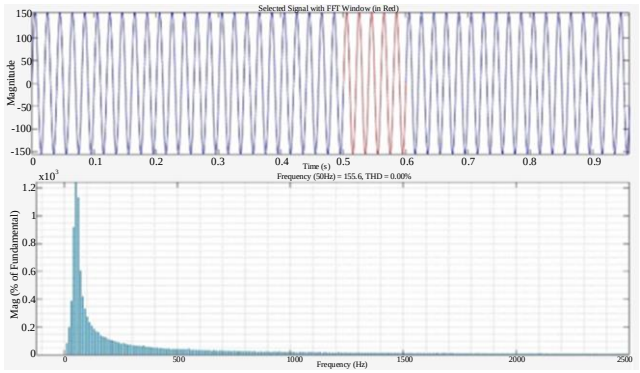

Fig. 29 Grid voltage THD (%) With proposed converter

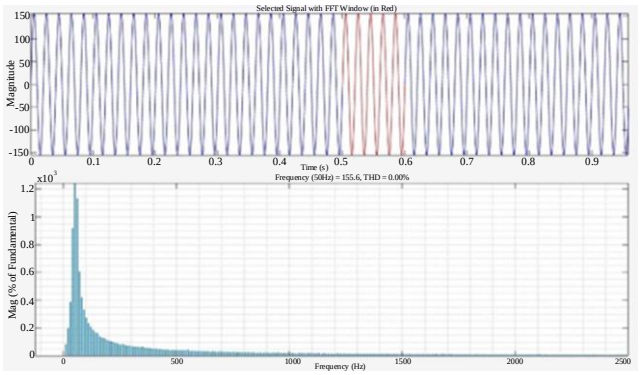

Fig. 30 Grid voltage THD (%) with SEPIC Converter

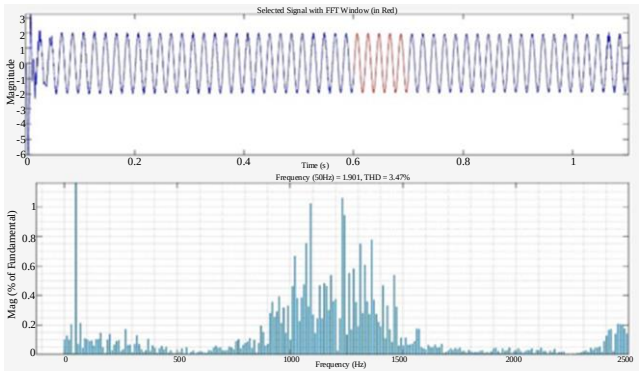

Fig. 31 Grid current THD (%) With proposed converter

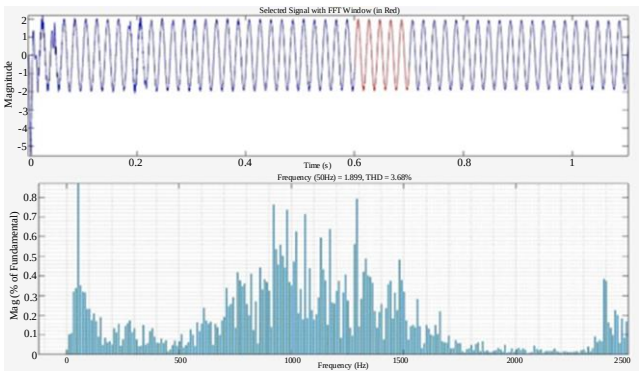

Fig. 32 Grid current THD (%) with SEPIC Converter

6. Conclusion

Based on the results obtained, it is concluded that the proposed converter operates efficiently within the HSWS. Utilizing the ZVS technique it demonstrates negligible switching losses and achieves an impressive efficiency of nearly 98%. In the solar system, the converter effectively boosts voltage from 120 V to 320 V (almost tripling), while in the wind system, it elevates voltage from 50 V to 320 V (nearly sixfold). The PSO-ANFIS MPPT controller accurately extracts maximum power from both solar and wind systems with swift tracking speed. It maintains solar output at the rated value of 1000 watts and wind output at 500 watts.

The battery system, coupled with a bidirectional converter, successfully maintains a constant voltage of 320 V at the DC-bus. The HSWS operates seamlessly in both standalone and grid-connected modes. It supplies power to DC loads (1000 watts) and AC loads (370 watts) in standalone mode. In grid-connected mode, it seamlessly integrates with the three-phase AC grid. Future research could focus on implementing an experimental system to assess the practical performance of the proposed converter. This would provide valuable insights into its real-world operation and further enhance its applicability.

Nomenclature

I_D	Diode current
V_t	Thermal voltage of the array
I_o	Diode saturation current
I_{PV}	Photovoltaic current
I_{sh}	Current through the shunt resistance
I_{sc}	Short circuit current
G, G_o	Incident solar irradiance, Nominal irradiance
E_g	Band gap energy of the semiconductor
T, T_n	Actual temperature, Nominal temperature
I_{rs}	Reverse saturation current of diode
n	Diode constant
C_p	Performance coefficient of the turbine
ω_{dq}, ω_r	Electrical angular speed, Mechanical angular speed
L_{sd}, L_{sq}	Inductances of stator
Ψ	Permanent flux
R_s	Resistance of stator
P	Number of poles
J	Combined inertia of the rotor and the wind turbine in (kg.m^2)
I_{sd}, I_{sq}	Direct and quadrature axis reactance
T_{em}	Electromagnetic torque
D_{Buck}, D_{Boost}	Buck mode, boost mode duty cycle
R_L, R_H	Low voltage and high voltage side resistance
L_{Buck}, L_{Boost}	Inductance for buck mode, boost mode

References

[1] J. Jurasz et al., "A Review on the Complementarity of Renewable Energy Sources: Concept, Metrics, Application and Future Research Directions," *Solar Energy*, vol. 195. pp. 703-724, 2020. [CrossRef] [Google Scholar] [Publisher Link]

[2] Bidyadhar Subudhi, and Raseswari Pradhan, "A Comparative Study on Maximum Power Point Tracking Techniques for Photovoltaic Power Systems," *IEEE Transactions on Sustainable Energy*, vol. 4, no. 1, pp. 89-98, 2013. [CrossRef] [Google Scholar] [Publisher Link]

[3] Ratnakar Babu Bollipo, Suresh Mikkili, and Praveen Kumar Bonthagorla, "Hybrid, Optimal, Intelligent and Classical PV MPPT Techniques: A Review," *CSEE Journal of Power and Energy Systems*, vol. 7, no. 1, pp. 9-33, 2021. [CrossRef] [Google Scholar] [Publisher Link]

[4] Neeraj Priyadarshi et al., "An Experimental Estimation of Hybrid ANFIS-PSO-Based MPPT for PV Grid Integration under Fluctuating Sun Irradiance," *IEEE Systems Journal*, vol. 14, no. 1, pp. 1218-1229, 2020. [CrossRef] [Google Scholar] [Publisher Link]

[5] Fabio Inocêncio Kravetz, and Roger Gules, "Soft-Switching High Static Gain Modified SEPIC Converter," *IEEE Journal of Emerging and Selected Topics in Power Electronics*, vol. 9, no. 6, pp. 6739-6747, 2021. [CrossRef] [Google Scholar] [Publisher Link]

[6] Wei Qian et al., "A Switched-Capacitor DC-DC Converter with High Voltage Gain and Reduced Component Rating and Count," *IEEE Transactions on Industry Applications*, vol. 48, no. 4, pp. 1397-1406, 2012. [CrossRef] [Google Scholar] [Publisher Link]

[7] Fei Li et al., "Coupled-Inductor-Inverse High Step-Up Converter," *IET Power Electronics*, vol. 11, no. 5, pp. 902-911, 2018. [CrossRef] [Google Scholar] [Publisher Link]

[8] Reza Ebrahimi et al., "Coupled-Inductor-Based High Step-Up DC-DC Converter," *IET Power Electronics*, vol. 12, no. 12, pp. 3093-3104, 2019. [CrossRef] [Google Scholar] [Publisher Link]

[9] Bing Xie et al., "Modeling and Control for a Three-Phase Interleaved Bidirectional DC-DC Energy Storage Converter," *2017 China International Electrical and Energy Conference (CIEEC)*, Beijing, China, pp. 153-158, 2017. [CrossRef] [Google Scholar] [Publisher Link]

[10] Sonu Kumar, C. Sethuraman, and G Chandru, "Design of Control Unit for Off-grid and Grid Connected Solar- Wind Hybrid System Suitable for Supplying Power to Both AC and DC Loads," *2021 6th International Conference on Recent Trends on Electronics, Information, Communication and Technology (RTEICT)*, Bangalore, India, pp. 331-338, 2021. [CrossRef] [Google Scholar] [Publisher Link]

[11] Jeevan Adhikari et al., "Modeling, Design, and Implementation of a Power Conversion System for Small-Scale High-Altitude Wind Power Generating System," *IEEE Transactions on Industry Applications*, vol. 53, no. 1, pp. 283-295, 2017. [CrossRef] [Google Scholar] [Publisher Link]

[12] Fan Wang et al., "Three-Phase Interleaved High Step-Up Bidirectional DC-DC Converter," *IET Power Electronics*, vol. 13, no. 12, pp. 2469-2480, 2020. [CrossRef] [Google Scholar] [Publisher Link]

Appendix

Table 1. Specifications of the HSWS

	Parameters	**Values**
Solar Panel (MODEL: GOLDIO72F335PY24)	Parallel String Series Strings	1 3
	Rated Power	335W
	V_{oc}	46.50V
	I_{sc}	9.26A
	V_{mp}	37.70V
	I_{mp}	8.90A
Wind Turbine	Cut in Speed	3m/sec
	Cut out Speed	58m/sec
	Total Power (3 Turbines Connected in Parallel)	3*143=429W
Permanent Magnet Synchronous Generator	Input Mechanical Power (P_m)	500 watts
Battery Bank	Number of Batteries (Series Connected)	12 units
	Total Voltage	144 V
	Nominal Capacity	26 Ah @ 20hr rate
Interleaved Bidirectional Converter	Rated Capacity	1000 W
	Switching Frequency	10 kHz
Inverter	Inverter Rating	1000 W
	Switching Frequency	15 kHz
Output LC Filter	Inductor, Capacitor	11.2 mH, 182 mF
Proposed Converter 1 (for Solar)	Rated Capacity	1000 W
	Switching Frequency	5 kHz
	Output Voltage	320 V
	Input Voltage	120 V
Proposed Converter 2 (for Wind)	Rated Capacity	1000 W
	Switching Frequency	5 kHz

	Output Voltage	320 V
	Input Voltage	50 V
	DC link Capacitance	493µF
DC-Load (R-Load)	Total Capacity	1000 W
AC-Load (3-Phase Induction Motor)	Power	370 W(0.5 HP)
AC Grid	Grid Voltage	110 V
	Grid Frequency	50 Hz